
Rotation Curve and Mass Distribution in the Galaxy from the Velocities of Objects at Distances up to 200 kpc

A.T. Bajkova and V.V. Bobylev

Pulkovo Astronomical Observatory, St. Petersburg, Russia

Abstract—Three three-component (bulge, disk, halo) model Galactic gravitational potentials differing by the expression for the dark matter halo are considered. The central (bulge) and disk components are described by the Miyamoto–Nagai expressions. The Allen–Santillán (I), Wilkinson–Evans (II), and Navarro–Frenk–White (III) models are used to describe the halo. A set of present-day observational data in the range of Galactocentric distances R from 0 to 200 kpc is used to refine the parameters of these models. For the Allen–Santillán model, a dimensionless coefficient γ has been included as a sought-for parameter for the first time. In the traditional and modified versions, $\gamma = 2.0$ and 6.3 , respectively. Both versions are considered in this paper. The model rotation curves have been fitted to the observed velocities by taking into account the constraints on the local matter density $\rho_{\odot} = 0.1M_{\odot} \text{ pc}^{-3}$ and the force $K_{z=1.1}/2\pi G = 77M_{\odot}\text{pc}^{-2}$ acting perpendicularly to the Galactic plane. The Galactic mass within a sphere of radius 50 kpc, $M_G(R \leq 50 \text{ kpc}) \approx (0.41 \pm 0.12) \times 10^{12}M_{\odot}$, is shown to satisfy all three models. The differences between the models become increasingly significant with increasing radius R . In model I, the Galactic mass within a sphere of radius 200 kpc at $\gamma = 2.0$ turns out to be greatest among the models considered, $M_G(R \leq 200 \text{ kpc}) = (1.45 \pm 0.30) \times 10^{12}M_{\odot}$, $M_G(R \leq 200 \text{ kpc}) = (1.29 \pm 0.14) \times 10^{12}M_{\odot}$ at $\gamma = 6.3$, and the smallest value has been found in model II, $M_G(R \leq 200 \text{ kpc}) = (0.61 \pm 0.12) \times 10^{12}M_{\odot}$. In our view, model III is the best one among those considered, because it ensures the smallest residual between the data and the constructed model rotation curve provided that the constraints on the local parameters hold with a high accuracy. Here, the Galactic mass is $M_G(R \leq 200 \text{ kpc}) = (0.75 \pm 0.19) \times 10^{12}M_{\odot}$. A comparative analysis with the models by Irrgang et al. (2013), including those using the integration of orbits for the two globular clusters NGC 104 and NGC 1851 as an example, has been performed. The third model is shown to have subjected to a significant improvement.

INTRODUCTION

When the dynamical properties of stars, globular clusters, or dwarf satellite galaxies of the Milky Way are studied, the construction of their Galactic orbits plays an important role. This requires having a good model of the Galactic gravitational potential. The Galactic rotation curve, the dependence of the circular rotation velocity of objects V_{circ} on their distance from the Galactic rotation axis R , provides an observational basis for the construction of such models.

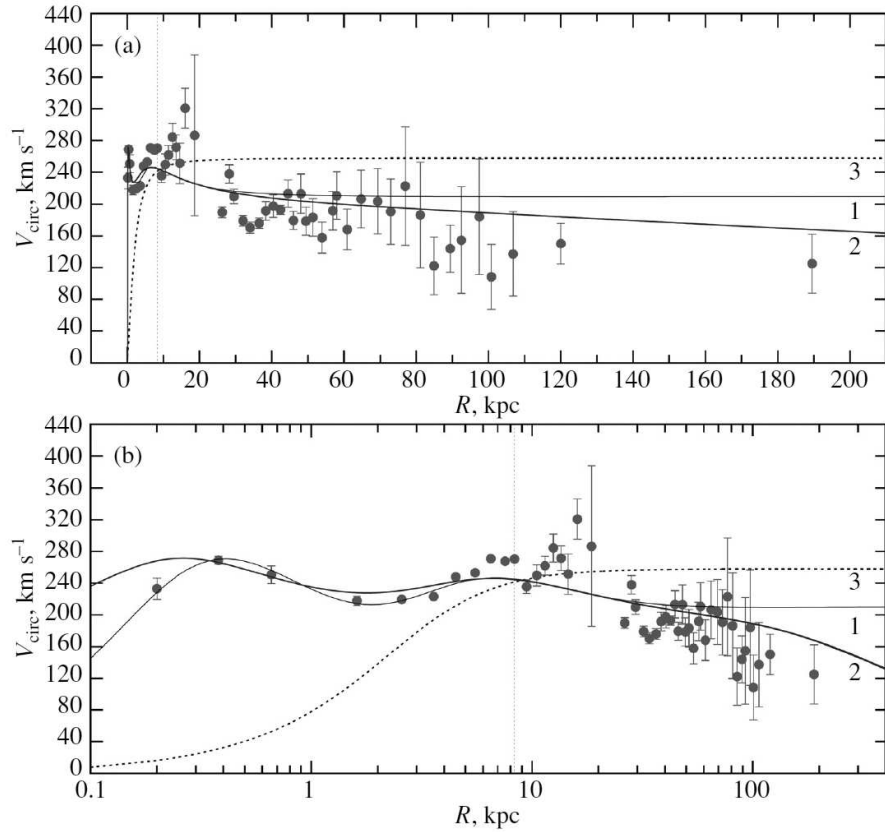


Figure 1: Galactic rotation curve: from Bhattacharjee et al. (2014), the filled circles with error bars; from Bobylev and Bajkova (2013), line 1; model II from Irrgang et al. (2013), line 2; from Gromov et al. (2015), line 3. The linear and logarithmic distance scales are on panels (a) and (b), respectively; the vertical line marks the Sun’s position.

At present, there are highly accurate velocities and distances only for the objects lying either close to the Sun or in the inner Galaxy ($R < R_{\odot}$). The Galactic rotation curve at greater distances from the rotation axis ($R \gg R_{\odot}$) is known with huge errors. The line-of-sight velocities of thick-disk and halo objects (carbon stars, horizontal-branch giants, globular clusters, dwarf satellite galaxies) are used (Sofue 2009, 2012; Bhattacharjee et al. 2014) in this region, but they have a large velocity dispersion and large errors in the distance estimates. Nevertheless, we know that the Galactic rotation curve does not remain flat but slowly falls off with increasing distance R . According to the calculations of various authors, the Galactic mass is either $M_G(R \leq 385 \text{ kpc}) = 0.70 \times 10^{12} M_{\odot}$ (Sofue 2012), or $M_G(R \leq 260 \text{ kpc}) = 1.37 \times 10^{12} M_{\odot}$ (Eadie et al. 2015), or even $M_G(R \leq 200 \text{ kpc}) = 3.0 \times 10^{12} M_{\odot}$ (model III in Irrgang et al. (2013)), i.e., the estimates differ by several times. The mass of the dark matter halo at such large radii will be a major contributor to the Galactic mass. For example, $M_H(R \leq 385 \text{ kpc}) = 0.65 \times 10^{12} M_{\odot}$ (Sofue 2012), where $R = 385 \text{ kpc}$ is half the distance between the Milky Way and the Andromeda Galaxy (M31).

The three-component model potential by Allen and Santillán (1991) is well known.

The orbits of various Galactic objects were determined by various authors using this model. For example, the orbits of dwarf galaxies (Lépine et al. 2011), globular clusters (Lane et al. 2012), planetary nebulae (Wu et al. 2011), and various stars (Edelmann et al. 2005; Pauli et al. 2006; Pereira et al. 2012) were determined. A number of modifications of the model by Allen and Santillán (1991), which differ by the halo shape (Navarro et al. 1997; Wilkinson and Evans 1999) or by the number of components (Gardner et al. 2011), are known.

Irrgang et al. (2013) and Bobylev and Bajkova (2013) refined the parameters of the Allen-Santillán model using the line-of-sight velocities of hydrogen clouds at the tangent points and the space velocities of Galactic masers with measured trigonometric parallaxes. The sample of masers with measured parallaxes currently provides the best basis for studying the Galactic thin disk (Reid et al. 2014). This is possible owing to the high accuracy of distance determinations, which is, on average, about 10%.

Figure 1 presents the Galactic rotation curve (in the form of averaged velocities) from Bhattacharjee et al. (2014), the two rotation curves found using masers from Bobylev and Bajkova (2013) and Irrgang et al. (2013), and the rotation curve found from hydrogen clouds by Gromov et al. (2015) using a quasiisothermal model potential. Out of the three models in Irrgang et al. (2013), we took model II where the rotation velocities fall off with distance faster than in the remaining models proposed by them. All three curves 1, 2, and 3 were found based on samples of objects located at distances $R < 20$ kpc.

As can be seen from the lower panel in Fig. 1, curves 1 and 2 are in good agreement with the observational data in the inner Galaxy ($R < R_{\odot}$). All three curves show considerable disagreement with the data at distances R greater than 30–40 kpc, which is clearly seen on both panels of Fig. 1. Based on this figure, we can reach an obvious conclusion about the necessity of improving the model potentials at great distances.

The goal of this paper is to refine the parameters of the model Galactic potentials using the Galactic rotation curve in the range 0–200 kpc. We consider three three-component axisymmetric model potentials (consisting of a bulge, a disk, and a dark matter halo) that differ by the halo shape, just as was considered previously by Irrgang et al. (2013). The practical considerations associated with the numerical integration of orbits, namely the mathematical simplicity and closeness of the analytical expressions ensuring a high speed of computations, which is especially important in implementing the Monte Carlo method to estimate the errors, served as a justification for the choice of models provided that they were all capable of reproducing well the observational data. Whereas Irrgang et al. (2013) used only the masers with measured trigonometric parallaxes up to distances $R < 20$ kpc as observational data, we add the velocities of objects considerably farther from the Galactic center to the data on masers. More specifically, at $20 < R < 200$ kpc we use the data from Bhattacharjee et al. (2014), in which almost all of the present-day kinematic measurements of objects located at great distances are reflected.

DATA

Bhattacharjee et al. (2014) constructed the Galactic rotation curve in the range of Galactocentric distances 0–200 kpc using various kinematic data. The line-of-sight velocities

of hydrogen clouds at the tangent points were taken in the inner Galaxy ($R \leq R_\odot$ kpc). These were the data on planetary nebulae, open star clusters, Cepheids, and carbon stars at distances up to $R \approx 20$ kpc, while the line-of-sight velocities of thick-disk and halo objects were used at distances up to $R \approx 200$ kpc: 1457 blue horizontal branch giants, 2227 K giants, 16 globular clusters, 28 distant halo giants, and 21 dwarf galaxies. It is important to note that Bhattacharjee et al. (2014) constructed the Galactic rotation curve with $R_\odot = 8.3$ kpc and $V_\odot = 244$ km s⁻¹. Estimates close to these values were obtained by Irrgang et al. (2013) when analyzing the masers with measured trigonometric parallaxes for three model potentials. Reid et al. (2014) estimated $R_\odot = 8.34 \pm 0.16$ kpc and $V_\odot = 240 \pm 8$ km s⁻¹ by analyzing the kinematics of Galactic masers, while Bobylev and Bajkova found $R_\odot = 8.3 \pm 0.2$ kpc and $V_\odot = 241 \pm 7$ km s⁻¹ from masers.

It is clearly seen from Fig. 1 that a number of points on the rotation curve from Bhattacharjee et al. (2014) near $R \approx 20$ kpc have a large dispersion and show an abrupt jump into the region of high velocities. We decided not to use these data, especially since Bhattacharjee et al. (2014) used the kinematic distance estimates (for example, for HII regions from Hou et al. (2009) and Urquhart et al. (2012)) for a number of objects from this range of distances.

As a result, we rely on the line-of-sight velocities of hydrogen clouds at the tangent points and the data on 130 masers with measured trigonometric parallaxes at distances R less than 25 kpc, and the rotation curve from Bhattacharjee et al. (2014) serves as the data at greater distances.

The following can be said in more detail about the sample of masers with measured trigonometric parallaxes. The VLBI measurements of 103 masers are described in the review of Reid et al. (2014). A number of publications by these authors devoted to the analysis of masers located in individual Galactic spiral arms appeared subsequently, with improved values of the measured parameters having been given for some of the masers. The papers by Wu et al. (2014), Choi et al. (2014), Sato et al. (2014), Hachisuka et al. (2015), and Sanna et al. (2014) are devoted to the analysis of masers in the Carina–Sagittarius arm, the Perseus arm, the Scutum arm, the Outer Arm, and the central region of the Galaxy, respectively; finally, the paper by Xue et al. (2013) devoted to the masers in the Local Arm was published slightly earlier.

After the addition of the most recent astrometric measurements of masers (Motogi et al. 2015; Burns et al. 2015), we obtained a sample containing the data on 130 sources. We did not include the masers located at distances $R < 4$ kpc in our sample, because the maser velocities here have large dispersions. The data on hydrogen clouds are better suited for this region. We use the line-of-sight velocities of HI clouds at the tangent points from the central region of the Galaxy (Burton and Gordon 1978). Note, finally, that the circular rotation velocities (V_{circ}) of masers were derived from their total space velocities, which increases considerably the reliability of these data. In contrast, when constructing the velocities of many other objects at distances $R > 25$ kpc, we used only their line-of-sight velocities.

MODEL POTENTIALS

Introductory Concepts

In all of the models here, the axisymmetric Galactic potential is represented as a sum of three components—a central spherical bulge $\Phi_b(r(R, z))$, a disk $\Phi_d(r(R, z))$, and a massive spherical dark matter halo $\Phi_h(r(R, z))$:

$$\Phi(R, z) = \Phi_b(r(R, z)) + \Phi_d(r(R, z)) + \Phi_h(r(R, z)). \quad (1)$$

We use a cylindrical coordinate system (R, ψ, z) with the coordinate origin at the Galactic center. In a rectangular coordinate system (x, y, z) with the coordinate origin at the Galactic center, the distance to a star (spherical radius) will be $r^2 = x^2 + y^2 + z^2 = R^2 + z^2$.

In accordance with the convention adopted in Allen and Santillán (1991), we express the gravitational potential in units of $100 \text{ km}^2 \text{ s}^{-2}$, the distances in kpc, and the masses in units of the Galactic mass $M_{gal} = 2.325 \times 10^7 M_\odot$, corresponding to the gravitational constant $G = 1$.

The expression for the mass density follows from the Poisson equation

$$4\pi G \rho(R, z) = \nabla^2 \Phi(R, z) \quad (2)$$

and is

$$\rho(R, z) = \frac{1}{4\pi G} \left(\frac{d^2 \Phi(R, z)}{dR^2} + \frac{1}{R} \frac{d\Phi(R, z)}{dR} + \frac{d^2 \Phi(R, z)}{dz^2} \right). \quad (3)$$

The force acting in the z direction perpendicularly to the Galactic plane is expressed as

$$K_z(z, R) = -\frac{d\Phi(z, R)}{dz}. \quad (4)$$

We will need Eqs. (3) and (4) below to solve the problem of fitting the parameters of the model gravitational potentials with constraints imposed on the local dynamical mass density ρ_\odot and the force $K_z(z, R_\odot)$ kpc, which are known from observations. In addition, we will need the expressions to calculate:

- (1) the circular velocities

$$V_{circ}(R) = \sqrt{R \frac{d\Phi(R, 0)}{dR}}, \quad (5)$$

- (2) the Galactic mass contained in a sphere of radius r

$$m(< r) = r^2 \frac{d\Phi(r)}{dr}, \quad (6)$$

- (3) the parabolic velocity or the escape velocity of a star from the attractive Galactic field

$$V_{esc}(R, z) = \sqrt{-2\Phi(R, z)}, \quad (7)$$

- (4) the Oort parameters

$$A = \frac{1}{2} R_\odot \Omega'_\odot, \quad (8)$$

$$B = \Omega_{\odot} + A, \quad (9)$$

where $\Omega = V/R$ is the angular velocity of Galactic rotation ($\Omega_{\odot} = V_{\odot}/R_{\odot}$), Ω' is the first derivative of the angular velocity with respect to R , and R_{\odot} is the Galactocentric distance of the Sun.

(5) the surface density of gravitating matter within z_{out} of the Galactic $z = 0$ plane

$$\Sigma_{out}(z_{out}) = 2 \int_0^{z_{out}} \rho(R, z) dz = \frac{K_z}{2\pi G} + \frac{2z_{out}(B^2 - A^2)}{2\pi G}, \quad (10)$$

Bulge and Disk

In all of the models being considered here, the bulge, $\Phi_b(r(R, z))$, and disk, $\Phi_d(r(R, z))$, potentials are represented in the form proposed by Miyamoto and Nagai (1975):

$$\Phi_b(r) = -\frac{M_b}{(r^2 + b_b^2)^{1/2}}, \quad (11)$$

$$\Phi_d(R, z) = -\frac{M_d}{\{R^2 + [a_d + (z^2 + b_d^2)^{1/2}]^2\}^{1/2}}, \quad (12)$$

where M_b and M_d are the masses of the components, b_b, a_d , and b_d are the scale lengths of the components in kpc. The corresponding expressions for the mass densities $\rho_b(R, z)$ and $\rho_d(R, z)$ are

$$\rho_b(r) = \frac{3b_b^2 M_b}{4\pi(r^2 + b_b^2)^{5/2}}, \quad (13)$$

$$\rho_d(R, z) = \frac{b_d^2 M_d}{4\pi(z^2 + b_d^2)^{3/2}} \frac{a_d R^2 + (a_d + 3\sqrt{z^2 + b_d^2})(a_d + \sqrt{z^2 + b_d^2})^2}{(R^2 + (a_d + \sqrt{z^2 + b_d^2})^2)^{5/2}}. \quad (14)$$

Expressions (11) and (13) are called a Plummer (1911) sphere, while relations (12) and (14) are called a generalized Kuzmin (1956) disk. Integrating the mass densities over the entire volume of the Galaxy gives the expected bulge and disk masses: $m_b = M_b, m_d = M_d$. The contributions of the bulge and the disk to the circular velocity are, respectively,

$$V_{circ(b)}^2(R) = \frac{M_b R^2}{(R^2 + b_b^2)^{3/2}}, \quad (15)$$

$$V_{circ(d)}^2(R) = \frac{M_d R^2}{(R^2 + (a_d + b_d)^2)^{3/2}}. \quad (16)$$

The corresponding expressions for $K_z^b(z, R)$ and $K_z^d(z, R)$ are

$$K_z^b(z, R) = \frac{zM_b}{(R^2 + z^2 + b_b^2)^{3/2}}, \quad (17)$$

$$K_z^d(z, R) = \frac{zM_d(a_d + \sqrt{z^2 + b_d^2})}{\sqrt{z^2 + b_d^2}(R^2 + (a_d + \sqrt{z^2 + b_d^2})^2)^{3/2}}. \quad (18)$$

Halo

Model I. The expression for the halo potential was derived by Irrgang et al. (2013) based on the expression for the halo mass from Allen and Martos (1986):

$$m_h(< r) = \left\{ \begin{array}{ll} \frac{M_h(r/a_h)^\gamma}{1 + (r/a_h)^{\gamma-1}}, & \text{if } r \leq \Lambda \\ \frac{M_h(\Lambda/a_h)^\gamma}{1 + (\Lambda/a_h)^{\gamma-1}} = \text{const}, & \text{if } r > \Lambda \end{array} \right\}, \quad (19)$$

It slightly differs from that given in Allen and Santillán (1991) and is

$$\Phi_h(r) = \left\{ \begin{array}{ll} \frac{M_h}{a_h} \left(\frac{1}{(\gamma-1)} \ln \left(\frac{1 + (r/a_h)^{\gamma-1}}{1 + (\Lambda/a_h)^{\gamma-1}} \right) - \frac{(\Lambda/a_h)^{\gamma-1}}{1 + (\Lambda/a_h)^{\gamma-1}} \right), & \text{if } r \leq \Lambda \\ -\frac{M_h}{r} \frac{(\Lambda/a_h)^\gamma}{1 + (\Lambda/a_h)^{\gamma-1}}, & \text{if } r > \Lambda, \end{array} \right. \quad (20)$$

where M_h is the mass, a_h is the scale length, the Galactocentric distance is $\Lambda = 200$ kpc, and the dimensionless coefficient $\gamma = 2.0$. The mass density is represented as

$$\rho_h(r) = \left\{ \begin{array}{ll} \frac{M_h}{4\pi a_h} \frac{(r/a_h)^{\gamma-1} ((r/a_h)^{\gamma-1} + \gamma)}{r^2 (1 + (r/a_h)^{\gamma-1})^2}, & \text{if } r \leq \Lambda. \\ 0, & \text{if } r > \Lambda. \end{array} \right. \quad (21)$$

The contribution of the halo to the circular velocity is

$$V_{\text{circ}(h)}^2(R) = \left\{ \begin{array}{ll} \frac{M_h R^{\gamma-1}}{a_h^\gamma (1 + (R/a_h)^{\gamma-1})}, & \text{if } r \leq \Lambda \\ \frac{M_h}{R} \frac{(\Lambda/a_h)^\gamma}{1 + (\Lambda/a_h)^{\gamma-1}}, & \text{if } r > \Lambda. \end{array} \right. \quad (22)$$

The expression for $K_z^h(z, R)$ at $r \leq \Lambda$ is

$$K_z^h(z, R) = \frac{zM_h(\sqrt{R^2 + z^2}/a_h)^{\gamma-1}}{a_h^2 \sqrt{R^2 + z^2} (1 + (\sqrt{R^2 + z^2}/a_h)^{\gamma-1})}. \quad (23)$$

Model II. The halo component is represented in the form proposed by Wilkinson and Evans (1999) as

$$\Phi_h(r) = -\frac{M_h}{a_h} \ln \left(\frac{a_h + \sqrt{r^2 + a_h^2}}{r} \right). \quad (24)$$

The mass density is calculated from the formula

$$\rho_h(r) = \frac{M_h}{4\pi} \frac{a_h^2}{r^2(r^2 + a_h^2)^{3/2}}. \quad (25)$$

The contribution of the halo to the circular velocity is

$$V_{circ(h)}^2(R) = \frac{M_h}{\sqrt{R^2 + a_h^2}}. \quad (26)$$

The expression for $K_z^h(z, R)$ is

$$K_z^h(z, R) = \frac{zM_h}{(R^2 + z^2)\sqrt{R^2 + z^2 + a_h^2}}. \quad (27)$$

Model III. The halo component is represented in the form proposed by Navarro et al. (1997) as

$$\Phi_h(r) = -\frac{M_h}{r} \ln\left(1 + \frac{r}{a_h}\right). \quad (28)$$

This model is often called the NFW (Navarro, Frenk, White) model. The corresponding mass density is

$$\rho_h(r) = \frac{M_h}{4\pi} \frac{1}{r(r + a_h)^2}. \quad (29)$$

The contribution to the circular velocity is

$$V_{circ(h)}^2(R) = M_h \left[\frac{\ln(1 + R/a_h)}{R} - \frac{1}{R + a_h} \right]. \quad (30)$$

The expression for $K_z^h(z, R)$ is

$$K_z^h(z, R) = \left| \frac{zM_h}{(R^2 + z^2)} \left(\frac{1}{a_h + \sqrt{R^2 + z^2}} - \frac{\ln(1 + \sqrt{R^2 + z^2}/a_h)}{\sqrt{R^2 + z^2}} \right) \right|. \quad (31)$$

Parameter Fitting

As follows from Bhattacharjee et al. (2014), the velocities of all objects on the Galactic rotation curve were calculated with $R_\odot = 8.3$ kpc and $V_\odot = 244$ km s⁻¹. The parameters of the model potentials I–III are found by least-squares fitting to the measured circular rotation velocities (V_{circ}) of Galactic objects. We applied the unit weights at which the smallest residual between the data and the rotation curve was achieved.

The local dynamical mass density ρ_\odot , which is the sum of the bulge, disk, and dark matter densities in a small solar neighborhood, together with the surface density $\Sigma_{1,1}$ are the most important additional constraints in the problem of fitting the parameters of the model potentials to the measured circular velocities (Irrgang et al. 2013):

$$\rho_\odot = \rho_b(R_\odot) + \rho_d(R_\odot) + \rho_h(R_\odot), \quad (32)$$

Table 1: The parameters of models I–III found by fitting to the data

Parameters	Model I, $\gamma = 2.0$	Model I, $\gamma = 6.3$	Model II	Model III
$M_b (M_g)$	386 ± 10	496 ± 19	142 ± 12	443 ± 27
$M_d (M_g)$	3092 ± 62	3200 ± 115	2732 ± 16	2798 ± 84
$M_h (M_g)$	452 ± 83	1396 ± 122	24572 ± 5459	12474 ± 3289
b_b (kpc)	0.2487 ± 0.0060	0.2809 ± 0.0077	0.2497 ± 0.0093	0.2672 ± 0.0090
a_d (kpc)	3.67 ± 0.16	3.12 ± 0.20	5.16 ± 0.32	4.40 ± 0.73
b_d (kpc)	0.3049 ± 0.0028	0.2929 ± 0.0046	0.3105 ± 0.0032	0.3084 ± 0.0050
a_h (kpc)	1.52 ± 0.18	5.39 ± 0.44	64.3 ± 15	7.7 ± 2.1
Entropy of res. noise E	-31.40	-26.51	-27.78	-24.51
δ (km s $^{-1}$)	15.7	14.1	13.8	13.1
δ_{irg} (km s $^{-1}$)	19.4	—	16.4	38.4

The Galactic mass unit is $M_g = 2.325 \times 10^7 M_\odot$.

$$\Sigma_{1.1} = \int_{-1.1 \text{ kpc}}^{1.1 \text{ kpc}} (\rho_b(R_\odot, z) + \rho_d(R_\odot, z) + \rho_h(R_\odot, z)) dz. \quad (33)$$

The surface density is closely related to the force $K_z(z, R)$ in accordance with Eq. (10). Since the two most important parameters ρ_\odot and $K_z/2\pi G$ are known from observations with a sufficiently high accuracy, introducing additional constraints on these two parameters allows the parameters of the gravitational potential to be refined significantly.

For example, according to the analysis of the distribution of stars from the Hipparcos Catalogue (1997) performed by Holmberg and Flynn (2000), $\rho_\odot = 0.102 \pm 0.010 M_\odot \text{ pc}^{-3}$. Values of ρ_\odot fairly close to this value were obtained subsequently from various data. For example, $\rho_\odot = 0.120_{-0.019}^{+0.016} M_\odot \text{ pc}^{-3}$ (Garbari et al. 2012), $\rho_\odot = 0.091 \pm 0.0056 M_\odot \text{ pc}^{-3}$ (Bienaymé et al. 2014), or $\rho_\odot = 0.097 \pm 0.013 M_\odot \text{ pc}^{-3}$ (McKee et al. 2015).

The estimates of the local surface density Σ are more difficult to compare, because this quantity depends on the adopted scale height and the limits of integration, which were taken to be different by different authors. For example, Korchagin et al. (2003) estimated $\Sigma_{0.35} = 42 \pm 6 M_\odot \text{ pc}^{-2}$ (here, $|z| \leq 0.35$ kpc) based on K-type giants from the Hipparcos Catalogue. Therefore, for a proper comparison of the results, we should extrapolate to the same range of heights, for example, to ± 1.1 kpc as in Eq. (10).

By analyzing the distribution of K giants in the solar neighborhood, Holmberg and Flynn (2004) estimated $\Sigma_{1.1} = 74 \pm 6 M_\odot \text{ pc}^{-2}$. Since Irrgang et al. (2013) relied on this estimate, the three model Galactic potentials constructed by them from hydrogen and masers have $\Sigma_{1.1} = 74 - 75 M_\odot \text{ pc}^{-2}$. Present-day estimations give slightly lower values of this parameter. For example, based on a sample of 9000 K stars with measured spectra from the SDSS/SEGUE catalogues, Zhang et al. (2013) estimated $\Sigma_{1.0} = 67 \pm 6 M_\odot \text{ pc}^{-2}$; Bovy and Rix (2013) found $\Sigma_{1.1} = 68 \pm 4 M_\odot \text{ pc}^{-2}$ based on 16300 G dwarfs from the SEGUE catalogue. A useful and comprehensive review of present-day local density determinations can be found in Reid (2014). In particular, a new summary estimate of the local surface density of baryons (HI, H₂, gas, stars, stellar remnants/brown dwarfs),

Table 2: The values of the quantities calculated from the parameters of models I–III found

Parameters	Model I, $\gamma = 2.0$	Model I, $\gamma = 6.3$	Model II	Model III
$(\rho_{\odot})_d$ ($M_{\odot} \text{ pc}^{-3}$)	0.092±0.010	0.090±0.010	0.090±0.010	0.089±0.011
$(\rho_{\odot})_h$ ($M_{\odot} \text{ pc}^{-3}$)	0.008±0.001	0.009±0.001	0.010±0.001	0.010±0.001
ρ_{\odot} ($M_{\odot} \text{ pc}^{-3}$)	0.100±0.010	0.100±0.010	0.100±0.010	0.100±0.010
$K_{z=1.1}/2\pi G$ ($M_{\odot} \text{ pc}^{-2}$)	77.2±6.9	77.0±7.1	77.01±10.2	77.1±12.5
$\Sigma_{1.1}$ ($M_{\odot} \text{ pc}^{-2}$)	71.4±7.3	71.9 ±8.1	75.78±10.1	76.8±12.3
Σ_{out} ($M_{\odot} \text{ pc}^{-2}$)	44.73±8.25	53.8 ±10.3	66.7±10.0	69.9±17.6
$V_{esc, R=R_{\odot}}$ (km s^{-1})	561.4 ±46.5	506.8 ±21.0	518.0±56.2	537.8±70.1
$V_{esc, R=200 \text{ kpc}}$ (km s^{-1})	250.0±25.6	115.5±5.0	164.4±16.0	210.6±26.2
V_{\odot} (km s^{-1})	239.0 ±12.0	245.0 ±7.6	242.5±28.0	243.9±34.5
A ($\text{km s}^{-1} \text{ kpc}^{-1}$)	16.01±0.80	15.89±0.72	15.11±1.84	15.04±2.37
B ($\text{km s}^{-1} \text{ kpc}^{-1}$)	-12.79 ±1.06	-13.64 ±0.89	-14.10±1.77	-14.35±2.12
$M_{G(R \leq 50 \text{ kpc})}$ ($10^{12} M_{\odot}$)	0.415±0.074	0.386 ±0.036	0.416±0.094	0.406±0.115
$M_{G(R \leq 100 \text{ kpc})}$ ($10^{12} M_{\odot}$)	0.760 ±0.149	0.686 ±0.072	0.546±0.108	0.570±0.153
$M_{G(R \leq 150 \text{ kpc})}$ ($10^{12} M_{\odot}$)	1.105 ±0.224	0.987 ±0.108	0.591±0.114	0.674±0.177
$M_{G(R < 200 \text{ kpc})}$ ($10^{12} M_{\odot}$)	1.450 ±0.300	1.288 ±0.144	0.609±0.117	0.750±0.194

$\Sigma_b = 54.2 \pm 4.9 M_{\odot} \text{ pc}^{-2}$, was obtained in this review.

We took the values from Irrgang et al. (2013) as the target parameters in fitting ρ_{\odot} and $K_{z=1.1}/2\pi G$. As a result, we used two additional constraints:

(i) the local matter density in the Galaxy ρ_{\odot} must be close to $\tilde{\rho}_{\odot} = 0.10 M_{\odot} \text{ pc}^{-3}$ known from observations (Holmberg and Flynn 2000);

(ii) the local force acting perpendicularly to the Galactic plane must be close to $\tilde{K}_{z=1.1}/2\pi G = 77 M_{\odot} \text{ pc}^{-2}$ at $R = R_{\odot}$, which corresponds to $\Sigma_{1.1} = 74 M_{\odot} \text{ pc}^{-2}$ found by Holmberg and Flynn (2004) from the observations of K giants in the solar neighborhood.

Thus, the parameter fitting problem was reduced to minimizing the following quadratic functional F :

$$\min F = \sum_{i=1}^N (V_{circ}(R_i) - \tilde{V}_{circ}(R_i))^2 + \alpha_1 (\rho_{\odot} - \tilde{\rho}_{\odot})^2 + \alpha_2 (K_{z=1.1}/2\pi G - \tilde{K}_{z=1.1}/2\pi G)^2, \quad (34)$$

where N is the number of data points; the tilde denotes the data from circular velocity measurements; R_i are the Galactocentric distances of the objects; α_1 and α_2 are the weight factors at the additional constraints that were chosen so as to minimize the residual between the data and the model rotation curve provided that the additional constraints hold with an accuracy of at least 5%. Based on the constructed models, we calculated the local surface density of the entire matter ρ_{\odot} and $K_{z=1.1}/2\pi G$ related to $\Sigma_{1.1}$ and Σ_{out} . The accuracies of all the parameters given in Tables 1 and 2 were determined through Monte Carlo simulations using each time 100 independent realizations of random measurement errors obeying a normal distribution with zero mean and a known rms deviation.

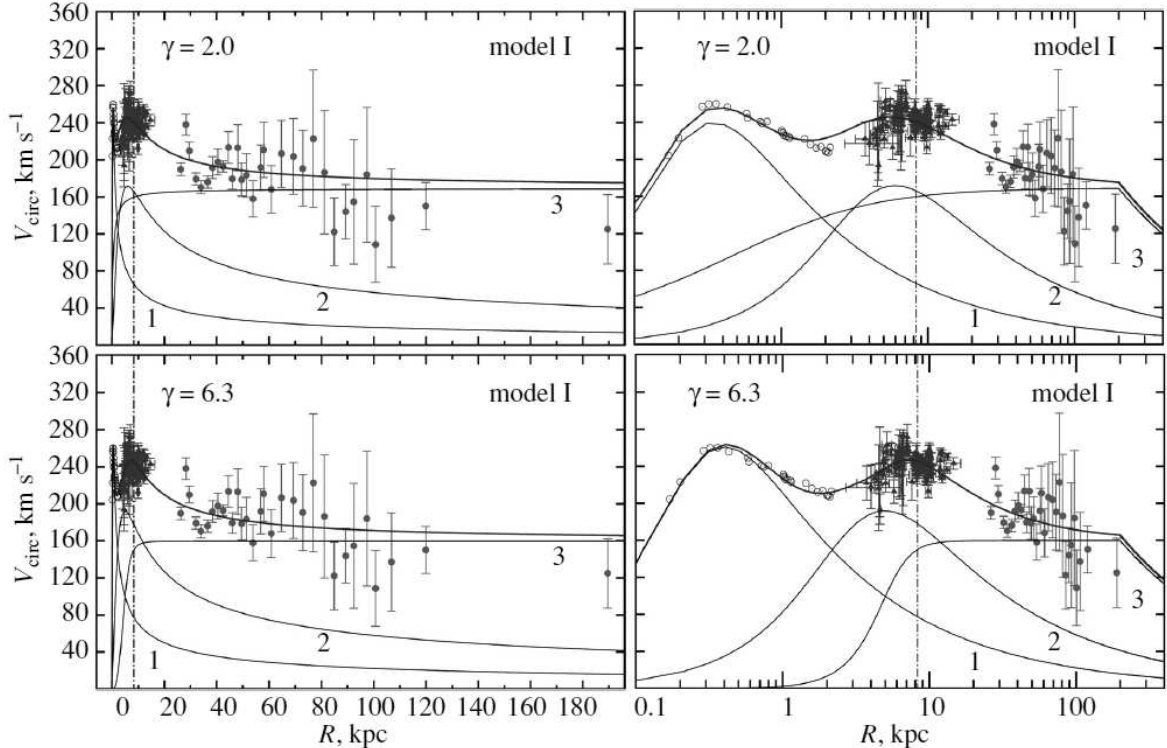


Figure 2: Galactic rotation curve for model I ($\gamma = 2.0$ and 6.3) in linear (left) and logarithmic (right) distance scales; the vertical line marks the Sun's position, numbers 1, 2, and 3 denote the bulge, disk, and halo contributions, respectively; the open circles, filled triangles, and filled circles indicate the HI velocities, the velocities of masers with measured trigonometric parallaxes, and the velocities from Bhattacharjee et al. (2014), respectively..

RESULTS

Table 1 provides the values of the seven sought for parameters ($M_b, M_d, M_h, b_b, a_d, a_b, a_h$) found by solving the fitting problem for the three model Galactic potentials under consideration. The next-to-last row in the table gives the residuals (in km s^{-1}) between the model rotation curve found and the circular velocities $\delta = \sqrt{\frac{1}{N} \left(\sum_{i=1}^N (V_{\text{circ}}(R_i) - \tilde{V}_{\text{circ}}(R_i))^2 \right)}$. As can be seen, model III provides the best fit to the data; model II yields a comparable result. For comparison, the last row gives the residuals between our data and the model rotation curves from Irrgang et al. (2013). It can be seen that the parameters we found provide a more accurate fit, especially in the case of model III (we managed to reduce the residual by a factor of 3).

Consider the first model separately. The mathematical description of the halo potential in this model contains one more parameter, the dimensionless coefficient γ . It was fixed at 2.02 in the model by Allen and Santillán (1991); $\gamma = 2.0$ in the model by Irrgang et al. (2013). In the first version of fitting the parameters of the potential, we also took

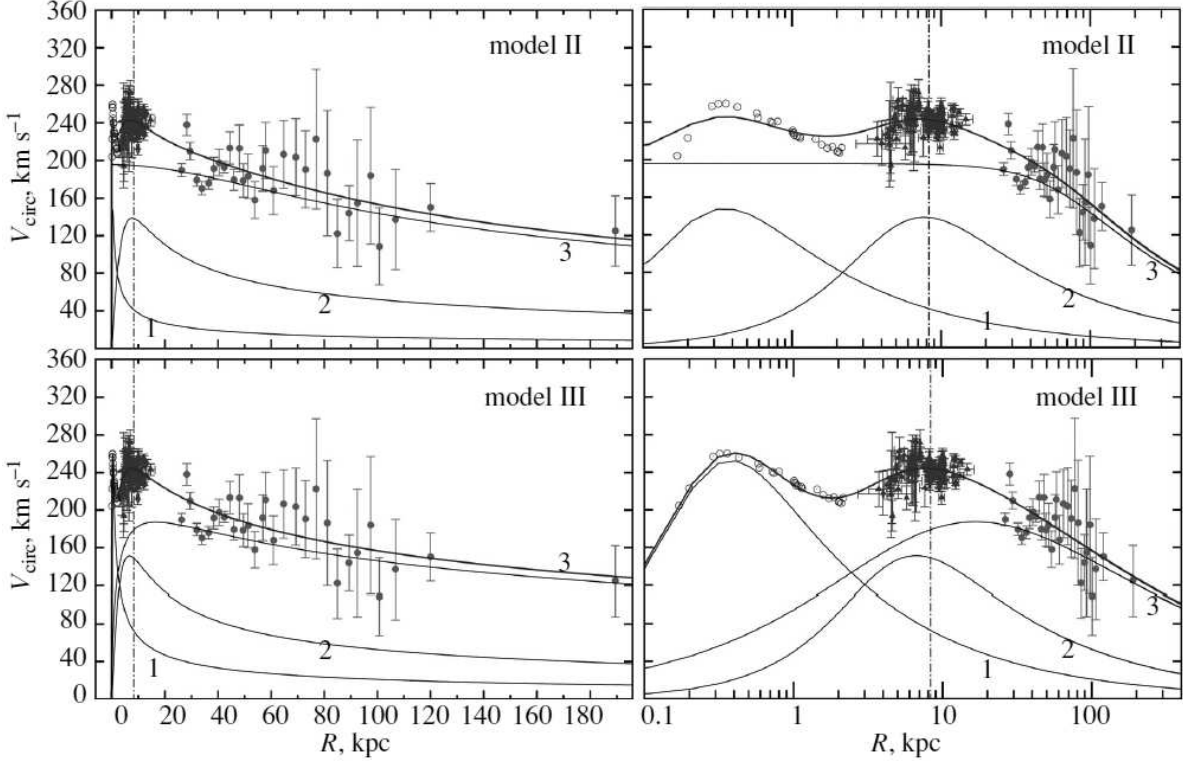


Figure 3: Galactic rotation curve for models II and III in linear (left) and logarithmic (right) distance scales; the vertical line marks the Sun’s position, numbers 1, 2, and 3 denote the bulge, disk, and halo contributions, respectively; the open circles, filled triangles, and filled circles indicate the HI velocities, the velocities of masers with measured trigonometric parallaxes, and the velocities from Bhattacharjee et al. (2014), respectively.

$\gamma = 2.0$. The results obtained are presented in the first column of Table 1. We see that the residual between the data and the constructed model rotation curve is tangibly larger than that in models II and III. In the second version of fitting, the coefficient γ was also included as a parameter being fitted. As a result, it turned out that the minimum value of the residual for the first model for our data was reached at $\gamma = 6.3$. The results of fitting other parameters are presented in the second column of Table 1. We see that the residual decreased noticeably.

To estimate the degree of uniformity of the residual noise (the difference between the data and the model rotation curve), we used the well-known concept of entropy calculated as follows:

$$E = -\frac{1}{N} \sum_{i=1}^N |\Delta_i| \ln(|\Delta_i|),$$

where $\Delta_i = V_{circ}(R_i) - \tilde{V}_{circ}(R_i)$. The higher the entropy, the more uniform the noise and, consequently, the better the parameter fitting. Obviously, the combination of δ and E gives a more comprehensive idea of the quality of fitting by various models than does δ alone. The entropy of the residual noise is given in Table 1. As we see, model III provides

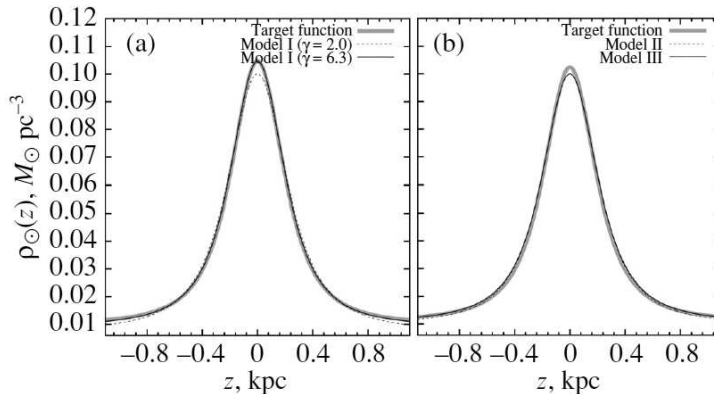


Figure 4: Results of fitting $\rho_{\odot}(z)$ for models I, II, and III. The functions from Irrgang et al. (2013) are considered as the target function $\rho_{\odot}(z)$.

the greatest entropy of the noise, i.e., its uniformity. Fitting the parameter γ allowed the entropy of the residual noise to be increased considerably in the first model as well.

Table 2 gives the physical quantities calculated from the derived parameters of the model potentials (Eqs. (1)–(31)). These include the local disk density $(\rho_{\odot})_d$ (the local bulge density is not given, because it is lower than the local disk density by several orders of magnitude), the local dark matter density $(\rho_{\odot})_h$, the local density of the entire matter ρ_{\odot} , the local surface density $\Sigma_{1.1}$ and Σ_{out} , the two escape velocities from the Galaxy V_{esc} (7) for $R = R_{\odot}$ and $R = 200$ kpc, the linear circular rotation velocity of the Sun V_{\odot} , the Oort constants A and B from Eqs. (8) and (9), and the Galactic mass M_G for four radii of the enclosing sphere. The Galactic rotation curves constructed for all of the models under consideration are presented in Figs. 2 and 3.

Let us perform a comparative analysis of the constructed model rotation curves.

In *model I*, the function describing the halo contribution to the velocity curve is a nondecreasing one, as can be clearly seen from Figs. 2 and 3. For this reason, the resulting model rotation curve describes poorly the data already at distances R greater than 120 kpc, the Galactic mass estimate at $R \leq 200$ kpc is greatest compared to the remaining models in this paper (the last rows in Table 2). However, it should be noted that model I at $\gamma = 6.3$ describes the data more accurately not only in the inner Galaxy, especially on masers and especially at $R = 2 - 8$ kpc (only the rotation curve of model III (Fig. 3) provides a similar fit to these data in this region), but also at great Galactocentric distances than that at $\gamma = 2.0$.

In *model II*, much of the mass in the inner Galaxy is accounted for by dark matter. As can be seen from Table 1, the lowest-mass central component corresponds to this model ($M_b = 142 \pm 12 M_g$). At present, the amount of dark matter in the inner Galactic region is being debated.

Whereas the presence of dark matter within the solar circle has been solidly established by Iocco et al (2015), and many analysis have aimed at the determination of its density profile in this region with different methods (e.g. Catena and Ullio (2010), Iocco et al. (2011), Bovy (2013), Pato et al. (2015), Pato and Iocco (2015); see Read (2014) for a

recent review), the innermost 2.5 kpc of the Galaxy is a more complicated region. In fact, the presence of a bar and the departure from sphericity of the shape of the bulge heavily hinder the reconstruction of dark matter component, which is also expected to play a subleading role in the total gravitational potential.

It can be concluded that although model II describes satisfactorily the Galactic rotation curve in the R range 0–200 kpc, it suggests the presence of a substantial dark matter mass in the inner region of the Galaxy ($R < R_\odot$), which is most likely far from reality.

Model III is currently one of the most commonly used models (see, e.g., Sofue 2009; Kafle et al. 2012; Deason et al. 2012a). In the outer Galaxy ($R > R_\odot$) its properties are similar to those of model II, while in the inner Galaxy ($R < R_\odot$) the dark matter mass is insignificant, which favorably distinguishes this model from model II. As can be seen from the next to- last row in Table 1, this model fits the data with the smallest residual δ and the greatest entropy of the residual noise.

Such local parameters of the rotation curve as the velocity V_\odot and the Oort constants A and B are satisfactorily reproduced by all three models considered.

Note that the escape velocities V_{esc} ($R = 200$ kpc) are usually approximately half those at $R = R_\odot$.

As has already been said, as the target parameters in fitting ρ_\odot and $K_{z=1.1}/2\pi G$ we took the values justified in Irrgang et al. (2013). Fitting these parameters basically led to fitting the function $\rho_\odot(z)$ and, consequently, in accordance with Eq. (33), the surface density $\Sigma_{1.1}$. The results of fitting to the function $\rho_\odot(z)$ obtained in Irrgang et al. (2013) and considered in this paper as a template are shown in Fig. 4. As can be seen from the figures, all of the models reproduce the required function $\rho_\odot(z)$ with a high accuracy. Model I with $\gamma = 6.3$ and model III provide the highest accuracy.

For an even subtler qualitative comparison of the constructed model Galactic potentials between themselves and with the models from Irrgang et al. (2013), we integrated the orbits of two globular clusters into the past, NGC 104 and NGC 1851, in time intervals of 400 Myr and 2 Gyr, respectively. The initial distances, proper motions, and line-of-sight velocities of the globular cluster NGC 104 were taken from Lane et al. (2012), where the HST (Hubble Space Telescope) proper motion measurements are provided. It should be noted that Table 1 from this paper gives $\mu_\alpha \cos(\delta)$, not just μ_α . The data for the globular cluster NGC 1851 were taken from the catalog by Kharchenko et al. (2013). The peculiar velocity of the Sun relative to the local standard of rest was taken to be $(U, V, W)_\odot = (11.1, 12.24, 7.25)$ km s⁻¹ (Schönrich et al. 2010). We assumed the velocity U to be directed toward the Galactic center, V to be in the direction of Galactic rotation, and W to be directed perpendicularly to the Galactic plane toward the North Galactic Pole. The orbits of NGC 104 and NGC 1851 in three planes (XY, XZ , and YZ) are presented in Figs. 5 and 6, respectively. To construct the orbits, we used the integrator of the equations of motion given in the Appendix to the paper by Irrgang et al. (2013) based on the fourth-order Runge–Kutta algorithm.

The first object (NGC 104) is characterized by comparatively low initial space velocities. In the Galactic coordinate system for model III, $(U, V, W) = (-77.4, 187.2, 35.1)$ km s⁻¹. Its orbit occupies a small region within < 8 kpc of the Galactic center. The second object (NGC 1851) has a considerably higher initial velocity in Z coordinate. In the Galactic coordinate system, $(U, V, W) = (-36.7, 102.5, -324.0)$ km s⁻¹. Its orbit encloses

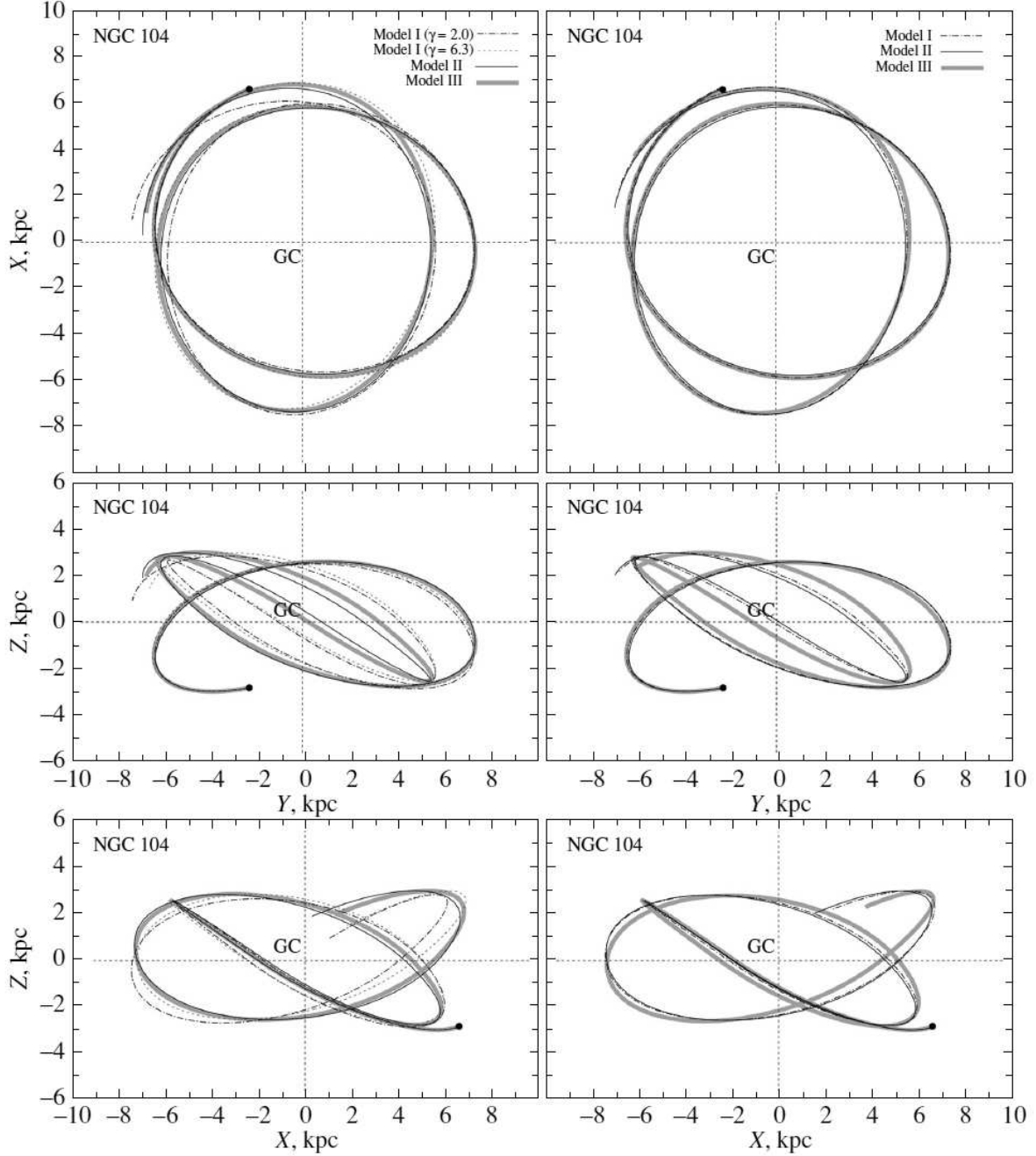


Figure 5: Orbits of the globular cluster NGC 104 in a time interval of 400 Myr in the past for models I, II, and III with the parameters derived in this paper (left) and the parameters from Irrgang et al. (2013) (right). The filled circle corresponds to the beginning of integration ($t = 0$).

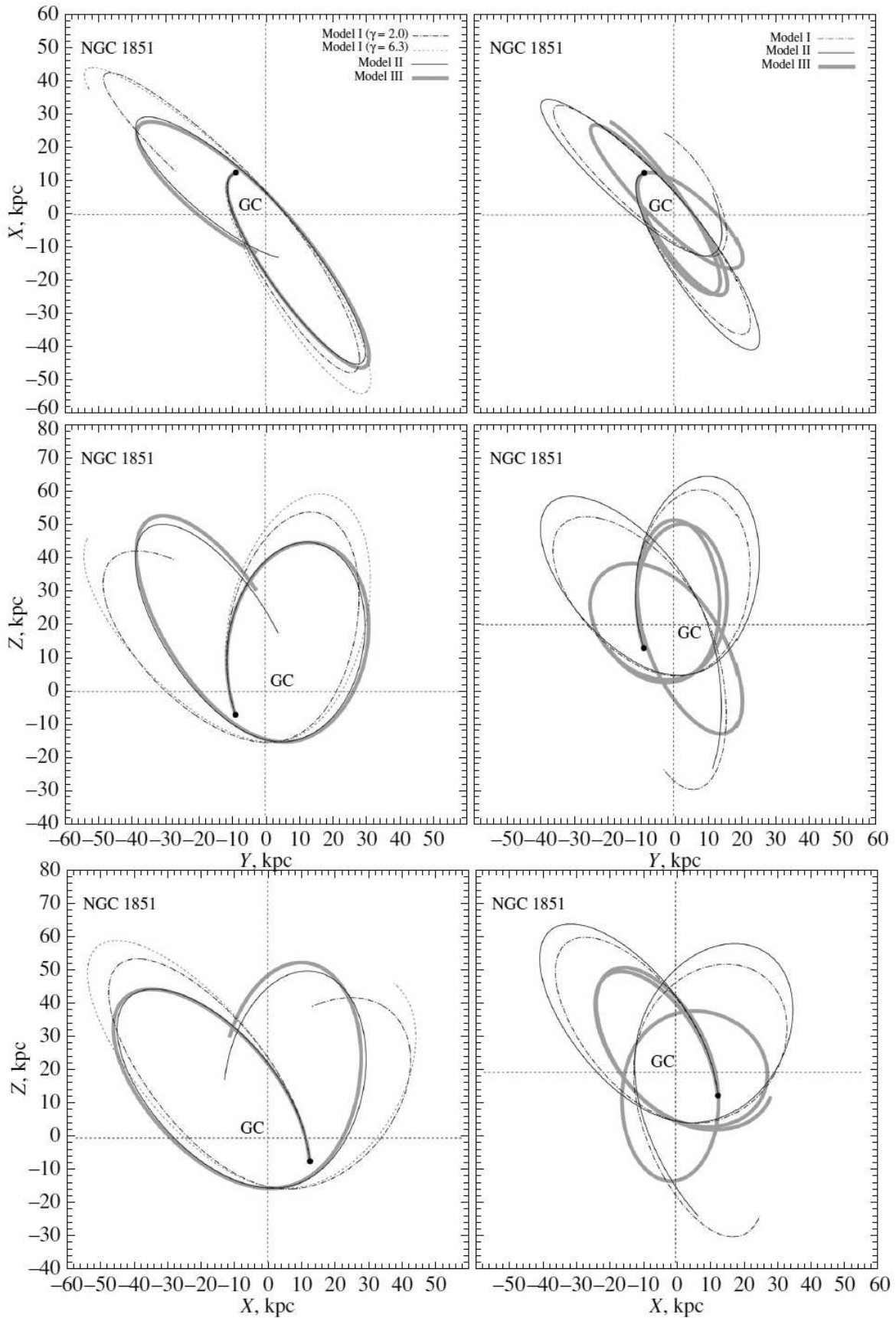


Figure 6: Orbits of the globular cluster NGC 1851 in a time interval of 2 Gyr in the past for models I, II, and III with the parameters derived in this paper (left) and the parameters

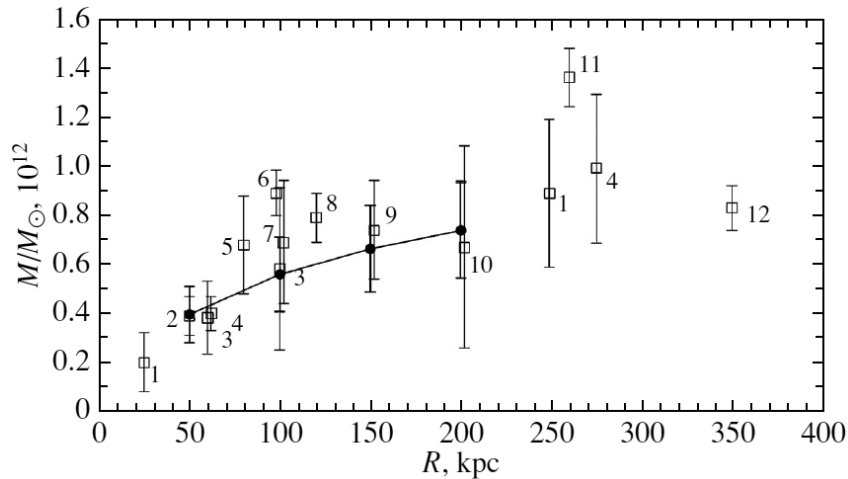


Figure 7: The galactic mass estimates obtained by various authors (open squares) and the estimates found in this paper based on model III (thick line); the numbers indicate the following sources: 1–Kafle et al. (2012), 2–Deason et al. (2012a), 3–Bhattacharjee et al. (2013), 4–Xue et al. (2008), 5–Gnedin et al. (2010), 6–McMillan (2011), 7–Dehnen and Binney (1998), 8–Battaglia et al. (2005), 9–Deason et al. (2012b), 10–Bhattacharjee et al. (2014), 11–Eadie et al. (2015), 12–Karachentsev et al. (2009).

a region with a radius up to 60 kpc over 2 Gyr. It was interesting for us to trace how the orbits behaved in different models at comparatively small and large Galactocentric distances.

The figures on the left and right panels correspond to our models and the models from Irrgang et al. (2013), respectively. It can be seen that the orbits of the first object corresponding to different models are fairly close to one another. It should be noted that our models I ($\gamma = 6.3$), II, and III give almost coincident orbits. The orbit corresponding to model I ($\gamma = 2.0$) slightly differs, so that model I with $\gamma = 6.3$ provides a closer orbit to the orbits from models II and III than does model I with $\gamma = 2.0$. As regards the models from Irrgang et al. (2013), models I and II provide the closest orbits between themselves.

The orbits from our models II and III for the second object, just as for the first object, almost coincide. The orbits constructed using models I differ noticeably. For the models with the parameters from Irrgang et al. (2013), it can be seen that the orbit from model III differs radically from the orbits of the two other models. The orbits from models I and II also differ between themselves, but only slightly. At the same time, they show a similarity to the orbits from our models II and III.

Thus, by fitting the data at great Galactocentric distances, we managed to significantly refine the parameters of all three models considered here, especially model III from Navarro et al. (1997). This enables a more accurate integration of the orbits of objects with high space velocities on long time scales.

DISCUSSION

Let us compare the parameters of models I–III from Tables 1 and 2 with the estimates by Irrgang et al. (2013). In addition, it is possible to compare the model rotation curves from model II using Figs. 1 and 2. There are minimal differences between models II. Our estimates of the mass parameters are always smaller. For example, the halo mass for this model $M_h = 69725 M_g$ from Irrgang et al. (2013) is approximately a factor of 3 greater than our value of $M_h = 24572 M_g$. For model III the difference in this parameter reaches already one order of magnitude. Nevertheless, the estimates of the Galactic mass M_G are quite close at $R \leq 50$ kpc and differ by a factor of 2 for model III. At $R \leq 200$ kpc the difference in M_G estimates is a factor of about 1.3 for model I, a factor of 2 for model II, and reaches a factor of 4 for model III. Indeed, for model III we found $M_G = (0.75 \pm 0.19) \times 10^{12} M_\odot$, while Irrgang et al. (2013) estimated $M_G = (3.0 \pm 1.1) \times 10^{12} M_\odot$.

Note once again that in Irrgang et al. (2013) the construction of model potentials was based on the observations of masers with measured trigonometric parallaxes located no farther than 20 kpc from the Galactic center. Therefore, it is of interest to compare our Galactic mass estimates with the results of other authors obtained from objects far from the Galactic center.

Such a problem was solved by Sofue (2012) on the basis of observational data in a wide range of distances $R : 0 - 1000$ kpc (Sofue 2009; Sofue et al. 2009, 2015). They are quite similar to those data that were used by Bhattacharjee et al. (2014), because they include the line-of-sight velocities of globular clusters and dwarf galaxies. Based on a three-component model potential with the dark matter halo represented in the NFW form (as in our model III), Sofue (2012) estimated $M_G(R \leq 385 \text{ kpc}) = (0.70 \pm 0.10) \times 10^{12} M_\odot$. A different estimate of this author is $M_G(R \leq 200 \text{ kpc}) = (0.70 \pm 0.51) \times 10^{12} M_\odot$ (Sofue 2015). Note that Bhattacharjee et al. (2014) estimated $M_G(R \leq 200 \text{ kpc}) = (0.68 \pm 0.41) \times 10^{12} M_\odot$. Thus, there is good agreement with the result of our model III $M_G(R \leq 200 \text{ kpc}) = (0.75 \pm 0.19) \times 10^{12} M_\odot$.

Xue et al. (2008) analyzed the line-of-sight velocities of blue horizontal-branch giants at distances $R < 60$ kpc. They constructed a three-component model potential in which the dark halo mass was represented in the NFW form, while the bulge and disk potentials differed from those we used. These authors estimated the virial mass of the Galaxy to be $M_G(R \leq R_{vir}) = (1.0^{+0.3}_{-0.2}) \times 10^{12} M_\odot$, where the virial radius was $R_{vir} = 275^{+23}_{-20}$ kpc. Here we can also see good agreement, within the error limits, with the estimate obtained in this paper based on model III.

Based on the velocities of globular clusters and dwarf galaxies at distances R up to 260 kpc, Eadie et al. (2015) estimated the Galactic mass to be $M_G(R \leq 260 \text{ kpc}) = (1.37 \pm 0.07) \times 10^{12} M_\odot$.

The Galactic mass within a sphere of radius 50 kpc, $M_G(R \leq 50 \text{ kpc}) \approx (0.41 \pm 0.12) \times 10^{12} M_\odot$, that we found based on three different model potentials is in good agreement with the results of other authors. For example, Deason et al. (2012a) estimate $M_G(R \leq 50 \text{ kpc}) = (0.42 \pm 0.04) \times 10^{12} M_\odot$; Williams and Evans (2015) found $M_G(R \leq 50 \text{ kpc}) = (0.45 \pm 0.15) \times 10^{12} M_\odot$ from the velocities of horizontal branch giants from the SDSS (Sloan Digital Sky Survey) catalogue.

Karachentsev et al. (2009) estimated the total mass of the Local Group to be $(1.9 \pm 0.2) \times 10^{12} M_{\odot}$ and the ratio of the Galactic and M31 masses to be 4:5. The effect of local Hubble flow deceleration and the distances and line-of-sight velocities of galaxies in the neighborhoods of the Local Group were used for this estimate. The total mass of the Galaxy obtained by this independent method is $M_G(R \leq 350 \text{ kpc}) = (0.84 \pm 0.09) \times 10^{12} M_{\odot}$, in complete agreement with our estimates.

Figure 7 presents the Galactic mass estimates obtained by different authors using different objects. Note that the results marked by numbers 1 and 4 at $R > 250 \text{ kpc}$ are the virial mass estimates, while the direct estimates were obtained from the data at $R < 80 \text{ kpc}$. On the whole, we can see good agreement of the estimates found in this paper based on model III with the results of different various.

CONCLUSIONS

We considered three three-component (bulge, disk, halo) model Galactic potentials differing by the shape of the dark matter halo. Present-day observational data spanning the range of Galactocentric distances R from 0 to $\sim 200 \text{ kpc}$ were used to refine the parameters of these models. We relied on the line-of-sight velocities of hydrogen clouds at the tangent points and the data on 130 masers with measured trigonometric parallaxes up to distances of about 20 kpc and used the averaged rotation velocities from Bhattacharjee et al. (2014) for greater distances.

In all of the models considered, the central component (bulge) and the Galactic disk are represented in the form of Miyamoto and Nagai (1975). The halo component is represented in the form of Allen and Martos (1986) and Allen and Santillán (1991) in model I, in the form of Wilkinson and Evans (1999) in model II, and in the form of Navarro et al. (1997) in model III.

For the Allen–Santillán model, a dimensionless coefficient γ has been included as a sought-for parameter for the first time. In the traditional version of model I, $\gamma = 2.0$. We obtained $\gamma = 6.3$, which allowed the fit to the circular velocity measurements by the model rotation curve to be improved noticeably. Both versions of the potential were analyzed.

We fitted the model rotation curve to the rotation velocities of Galactic objects known from observations by taking into account the additional constraints on (a) the local matter density ρ_{\odot} and the force $K_{z=1.1}$ acting perpendicularly to the Galactic plane. As a result, we obtained the model potentials that described a stellar system consistent with the physical characteristics of visible matter in the Galaxy known from observations.

The Galactic mass within a sphere of radius 50 kpc, $M_G(R \leq 50 \text{ kpc}) \approx (0.41 \pm 0.12) \times 10^{12} M_{\odot}$, was shown to satisfy all three models. The differences between the models become increasingly significant with increasing radius R . In model I, the Galactic mass within a sphere of radius 200 kpc at $\gamma = 2.0$ turns out to be greatest among the models considered, $M_G(R \leq 200 \text{ kpc}) = (1.45 \pm 0.30) \times 10^{12} M_{\odot}$, $M_G(R \leq 200 \text{ kpc}) = (1.29 \pm 0.14) \times 10^{12} M_{\odot}$, at $\gamma = 6.3$, and the smallest value was found in model II, $M_G(R \leq 200 \text{ kpc}) = (0.61 \pm 0.12) \times 10^{12} M_{\odot}$. In our view, model III (Navarro et al. 1997) is the best one among those considered, because it ensures the smallest residual between the data and the constructed model rotation curve provided that the constraints on the local parameters hold with a

high accuracy. Here, the Galactic mass is $M_G (R \leq 200 \text{ kpc}) = (0.75 \pm 0.19) \times 10^{12} M_\odot$.

A comparative analysis with the models by Irrgang et al. (2013), including those using the integration of orbits for the two globular clusters NGC 104 and NGC 1851 as an example, has been performed. The third model is shown to have been subjected to a significant improvement.

ACKNOWLEDGMENTS

We are grateful to the referees for their helpful remarks that contributed to an improvement of this paper. This work was supported by the “Transitional and Explosive Processes in Astrophysics” Program P-41 of the Presidium of Russian Academy of Sciences.

REFERENCES

1. C. Allen and M.A. Martos, *Rev. Mex. Astron. Astrofis.* 13, 137 (1986).
2. C. Allen and A. Santillán, *Rev. Mex. Astron. Astrofis.* 22, 255 (1991).
3. G. Battaglia, A. Helmi, H. Morrison, P. Harding, E.W. Olszewski, M. Mateo, K.C. Freeman, J. Norris, and S.A. Szechtman, *Mon. Not. R. Astron. Soc.* 364, 433 (2005).
4. P. Bhattacharjee, S. Chaudhury, S. Kundu, and S. Majumdar, *Phys. Rev. D* 87, 083525 (2013).
5. P. Bhattacharjee, S. Chaudhury, and S. Kundu, *Astrophys. J.* 785, 63 (2014).
6. O. Bienaymé, B. Famaey, A. Siebert, K.C. Freeman, B.K. Gibson, G. Gilmore, E.K. Grebel, J. Bland-Hawthorn, et al., *Astron. Astrophys.* 571, AA92 (2014).
7. V.V. Bobylev and A.T. Bajkova, *Astron. Lett.* 39, 809 (2013).
8. V.V. Bobylev and A.T. Bajkova, *Astron. Lett.* 40, 389 (2014).
9. J. Bovy, *Probes of Dark Matter on Galaxy Scales*, AAS Topical Conference Series Vol. 1. Proc. of conf. 14–19 July 2013 in Monterey, CA. *Bull. American Astron. Soc.*, 45, #7, #402.01 (2013).
10. J. Bovy and H.-W. Rix, *Astrophys. J.* 779, 115 (2013).
11. R.A. Burns, H. Imai, T. Handa, T. Omodaka, A. Nakagawa, T. Nagayama, and Y. Ueno, *Mon. Not. R. Astron. Soc.* 453, 3163 (2015).
12. W.B. Burton and M.A. Gordon, *Astron. Astrophys.* 63, 7 (1978).
13. R. Catena, and P. Ullio, *J. Cosmol. Astropart. Phys.* 8, 4 (2010).
14. Y.K. Choi, K. Hachisuka, M.J. Reid, Y. Xu, A. Brunthaler, K. M. Menten, and T.M. Dame, *Astrophys. J.* 790, 99 (2014).
15. A.J. Deason, V. Belokurov, N.W. Evans, and J. An, *Mon. Not. R. Astron. Soc.* 424, L44 (2012a).
16. A.J. Deason, V. Belokurov, N.W. Evans, S.E. Koposov, R.J. Cooke, J. Penarrubia, C.F.P. Laporte, M. Fellhauer, et al., *Mon. Not. R. Astron. Soc.* 425, 2840 (2012b).
17. W. Dehnen and J. Binney, *Mon. Not. R. Astron. Soc.* 294, 429 (1998).
18. G.M. Eadie, W.E. Harris, and L.M. Widrow, *Astrophys. J.* 806, 54 (2015).
19. H. Edelmann, R. Napiwotzki, U. Heber, N. Christlieb, and D. Reimers, *Astrophys. J.* 634, L181 (2005).
20. S. Garbari, C. Liu, J. I. Read, and G. Lake, *Mon. Not. R. Astron. Soc.* 425, 1445 (2012).
21. E. Gardner, P. Nurmi, C. Flynn, and S. Mikkola, *Mon. Not. R. Astron. Soc.* 411, 947 (2011).

22. O.Y. Gnedin, W.R. Brown, M.J. Geller, and S.J. Kenyon, *Astrophys. J.* 720, L108 (2010).
23. A.O. Gromov, I.I. Nikiforov, and L.P. Ossipkov, arXiv:1508.05298 (2015).
24. K. Hachisuka, Y.K. Choi, M.J. Reid, A. Brunthaler, K.M. Menten, A. Sanna, and T.M. Dame, *Astrophys. J.* 800, 2 (2015).
25. J. Holmberg and C. Flynn, *Mon. Not. R. Astron. Soc.* 313, 209 (2000).
26. J. Holmberg and C. Flynn, *Mon. Not. R. Astron. Soc.* 352, 440 (2004).
27. L.G. Hou, J.L. Han, and W.B. Shi, *Astron. Astrophys.* 499, 473 (2009).
28. F. Iocco, M. Pato, G. Bertone, and P. Jetzer, *J. Cosmol. Astropart. Phys.* 11, 29 (2011).
29. F. Iocco, M. Pato, and G. Bertone, *Nat. Phys.* 11, 245 (2015).
30. A. Irrgang, B. Wilcox, E. Tucker, and L. Schiefelbein, *Astron. Astrophys.* 549, 137 (2013).
31. R.R. Kaffe, S. Sharma, G.F. Lewis, and J. Bland-Hawthorn, *Astrophys. J.* 761, 98 (2012).
32. I.D. Karachentsev, O.G. Kashibadze, D.I. Makarov, and R.B. Tully, *Mon. Not. R. Astron. Soc.* 393, 1265 (2009).
33. N.V. Kharchenko, A.E. Piskunov, E. Schilbach, S. Röser, and R.-D. Scholz, *Astron. Astrophys.* 558, A53 (2013).
34. V.I. Korchagin, T.M. Girard, T.V. Borkova, D.T. Dinescu, and W.F. van Altena, *Astron. J.* 126, 2896 (2003).
35. G.G. Kuzmin, *Astron. Zh.* 33, 27 (1956).
36. R.R. Lane, A.H.W. Küpper, and D.C. Heggie, *Mon. Not. R. Astron. Soc.* 423, 2845 (2012).
37. S. Lépine, A. Koch, R.M. Rich, and K. Kuijken, *Astrophys. J.* 741, 100 (2011).
38. C.F. McKee, A. Parravano, and D.J. Hollenbach, *Astrophys. J.* 814, 13 (2015).
39. P.J. McMillan, *Mon. Not. R. Astron. Soc.* 414, 2446 (2011).
40. M. Miyamoto and R. Nagai, *Publ. Astron. Soc. Jpn.* 27, 533 (1975).
41. K. Motogi, K. Sorai, M. Honma, T. Hirota, K. Hachisuka, K. Niinuma, K. Sugiyama, Y. Yonekura, and K. Fujisawa, arXiv:1502.00376 (2015).
42. J.F. Navarro, C.S. Frenk, and S.D.M. White, *Astrophys. J.* 490, 493 (1997).
43. M. Pato and F. Iocco, *Astrophys. J.* 803, 3 (2015).
44. M. Pato, F. Iocco, and G. Bertone, *J. Cosmol. Astropart. Phys.* 12, 1 (2015).
45. E.-M. Pauli, R. Napiwotzki, U. Heber, M. Altmann, and M. Odenkirchen, *Astron. Astrophys.* 447, 173 (2006).
46. C.B. Pereira, E. Jilinski, N.A. Drake, D.B. de Castro, V.G. Ortega, C. Chavero, and F. Roig, *Astron. Astrophys.* 543, A58 (2012).
47. H.C. Plummer, *Mon. Not. R. Astron. Soc.* 71, 460 (1911).
48. J.I. Read, *J. Phys. G: Nucl. Part. Phys.* 41, f3101 (2014).
49. M.J. Reid, K.M. Menten, A. Brunthaler, X.W. Zheng, T.M. Dame, Y. Xu, Y. Wu, B. Zhang, et al., *Astrophys. J.* 783, 130 (2014).
50. A. Sanna, M.J. Reid, K.M. Menten, T.M. Dame, B. Zhang, M. Sato, A. Brunthaler, L. Moscadelli, and K. Immer, *Astrophys. J.* 781, 108 (2014).
51. M. Sato, Y.W. Wu, K. Immer, B. Zhang, A. Sanna, M.J. Reid, T. M. Dame, A. Brunthaler, and K.M. Menten, *Astrophys. J.* 793, 72 (2014).
52. R. Schönrich, J. Binney, and W. Dehnen, *Mon. Not. R. Astron. Soc.* 403, 1829 (2010).
53. Y. Sofue, *Publ. Astron. Soc. Jpn.* 61, 153 (2009).
54. Y. Sofue, M. Honma, and T. Omodaka, *Publ. Astron. Soc. Jpn.* 61, 227 (2009).
55. Y. Sofue, *Publ. Astron. Soc. Jpn.* 64, 75 (2012).

56. Y. Sofue, *Publ. Astron. Soc. Jpn.* 67, 75 (2015).
57. J.S. Urquhart, M.G. Hoare, S.L. Lumsden, R.D. Oudmaijer, T.J. T. Moore, J.C. Mottram, H.D.B. Cooper, M. Mottram, and H.C. Rogers, *Mon. Not. R. Astron. Soc.* 420, 1656 (2012).
58. M.I. Wilkinson and N.W. Evans, *Mon. Not. R. Astron. Soc.* 310, 645 (1999).
59. A.A. Williams and N.W. Evans, *Mon. Not. R. Astron. Soc.* 454, 698 (2015).
60. Z.-Y. Wu, J. Ma, X. Zhou, and C.-H. Du, *Astron. J.* 141, 104 (2011).
61. Y.W. Wu, M. Sato, M.J. Reid, L. Moscadelli, B. Zhang, Y. Xu, A. Brunthaler, K.M. Menten, T.M. Dame, and X.W. Zheng, *Astron. Astrophys.* 566, 17 (2014).
62. Y. Xu, J.J. Li, M.J. Reid, K.M. Menten, X.W. Zheng, A. Brunthaler, L. Moscadelli, T.M. Dame, and B. Zhang, *Astrophys. J.* 769, 15 (2013).
63. X.X. Xue, H.-W. Rix, G. Zhao, P. Re Fiorentin, T. Naab, M. Steinmetz, F.C. van den Bosch, et al., *Astrophys. J.* 684, 1143 (2008).
64. L. Zhang, H.-W. Rix, G. van de Ven, J. Bovy, C. Liu, and G. Zhao, *Astrophys. J.* 772, 108 (2013).
65. The Hipparcos and Tycho Catalogues, ESA SP- 1200 (1997).